



HAL
open science

Listening to laser sparks: a link between Laser-Induced Breakdown Spectroscopy, acoustic measurements and crater morphology

Baptiste Chide, Sylvestre Maurice, Naomi Murdoch, Jérémie Lasue, Bruno Bousquet, Xavier Jacob, Agnès Cousin, Olivier Forni, Olivier Gasnault, Pierre-Yves Meslin, et al.

► To cite this version:

Baptiste Chide, Sylvestre Maurice, Naomi Murdoch, Jérémie Lasue, Bruno Bousquet, et al.. Listening to laser sparks: a link between Laser-Induced Breakdown Spectroscopy, acoustic measurements and crater morphology. *Spectrochimica Acta Part B: Atomic Spectroscopy*, 2019, 153, pp.50-60. 10.1016/j.sab.2019.01.008 . hal-02028808

HAL Id: hal-02028808

<https://hal.science/hal-02028808>

Submitted on 20 Feb 2019

HAL is a multi-disciplinary open access archive for the deposit and dissemination of scientific research documents, whether they are published or not. The documents may come from teaching and research institutions in France or abroad, or from public or private research centers.

L'archive ouverte pluridisciplinaire **HAL**, est destinée au dépôt et à la diffusion de documents scientifiques de niveau recherche, publiés ou non, émanant des établissements d'enseignement et de recherche français ou étrangers, des laboratoires publics ou privés.



Open Archive Toulouse Archive Ouverte (OATAO)

OATAO is an open access repository that collects the work of some Toulouse researchers and makes it freely available over the web where possible.

This is an author's version published in: <https://oatao.univ-toulouse.fr/22764>

Official URL: <https://doi.org/10.1016/j.sab.2019.01.008>

To cite this version :

Chide, Baptiste and Maurice, Sylvestre and Murdoch, Naomi and Lasue, Jérémie and Bousquet, Bruno and Jacob, Xavier and Cousin, Agnès and Forni, Olivier and Gasnault, Olivier and Meslin, Pierre-Yves and Fronton, Jean-François and Bassas-Portús, Marti and Cadu, Alexandre and Sournac, Anthony and Mimoun, David and Wiens, Roger C. Listening to laser sparks: a link between Laser-Induced Breakdown Spectroscopy, acoustic measurements and crater morphology. (2019) Spectrochimica Acta Part B: Atomic Spectroscopy, 153. 50-60. ISSN 0584-8547

Any correspondence concerning this service should be sent to the repository administrator:

tech-oatao@listes-diff.inp-toulouse.fr

Listening to laser sparks: a link between Laser-Induced Breakdown Spectroscopy, acoustic measurements and crater morphology

Baptiste Chide^{a,b,*}, Sylvestre Maurice^b, Naomi Murdoch^a, Jérémie Lasue^b, Bruno Bousquet^c, Xavier Jacob^d, Agnès Cousin^b, Olivier Forni^b, Olivier Gasnault^b, Pierre-Yves Meslin^b, Jean-François Fronton^e, Marti Bassas-Portús^a, Alexandre Cadu^a, Anthony Sournac^a, David Mimoun^a, Roger C. Wiens^f

^a Institut Supérieur de l'Aéronautique et de l'Espace (ISAE-SUPAERO), Université de Toulouse, 31400 Toulouse, France

^b IRAP-CNRS, Université Toulouse III, 31400 Toulouse, France

^c Université de Bordeaux, CELIA, CNRS UMR 5107, 33400 Talence, France

^d IMFT – CNRS, Université Toulouse III, 31400 Toulouse, France

^e Centre National d'Etudes Spatiales (CNES), 31400 Toulouse, France

^f Los Alamos National Laboratory, Los Alamos, NM 87545, USA

ABSTRACT

Keywords:

SuperCam

Mars Microphone

LIBS

Acoustic

Shock-waves

Depth profile

Crater morphology

Ablated volume

In preparation for the SuperCam/Mars Microphone scientific investigation, the acoustic signal associated with the plasma formation during Laser-Induced Breakdown Spectroscopy (LIBS) experiment is studied with regard to the shot-to-shot evolution of the laser induced crater morphology and plasma emission lines. A set of geological targets are depth profiled using a specifically designed LIBS setup coupled with acoustic test bench under ambient terrestrial atmosphere. Experiments confirm that the decrease of the acoustic energy as a function of the number of shots is well correlated with the target hardness/density and also demonstrate that the acoustic energy can be used as a remote tracer of the ablated volume of the target. Listening to LIBS sparks provides a new information relative to the ablation process that is independent from the LIBS spectrum.

1. Introduction

Laser-Induced Breakdown Spectroscopy (LIBS) is an analytical technique that can remotely measure abundances of chemical elements in fluids and solids. This fast, precise, accurate, and non-intrusive method allows LIBS to be used in multiple applications in the lab and in situ to monitor aerosols in gas, study the contamination of soils, probe the level of radioactive elements [1] and more recently, to help space exploration by the study of planetary surfaces, to name only a few.

The LIBS technique was used for the first time in planetary exploration in 2012 as part of the ChemCam investigation onboard the NASA Curiosity rover [2,3]. Since landing at Gale crater, ChemCam has fired more than 600,000 laser shots on targets at distances of 1.5 m up to 9 m from the instrument. The typical measurement sequence consists of a series of 30 shots at the same point on a target. When firing the laser 150 times or more at the same location, ChemCam also has the capability to probe rocks at depth in order to study alteration rinds and coatings [4]. However, the evolution of the depth that is reached as a

function of the number of shots cannot be a priori determined on Mars from ChemCam measurements. The issue was briefly addressed in the laboratory only for two solid samples: a dolomite sandstone and a pressed pellet of Martian soil analog [5]. For these two types of target, the laser ablates ~400 μm after 300 shots with a rapid growth of the crater for the first 100 shots followed by a low ablative regime to reach the maximal depth. Nevertheless the number of targets tested and the small variety of their physical properties make difficult the extrapolation to other geological targets on Mars.

As an advancement of the ChemCam design, the SuperCam instrument suite selected for the NASA Mars 2020 rover will use LIBS but with the addition of Raman Spectroscopy and Visible and Infrared Reflectance Spectroscopy to determine the elemental composition and mineralogy of Mars soils and rocks [6]. The LIBS investigation will be supported by the Mars Microphone that will record LIBS shock-waves at distances up to 4 m [7]. The Mars Microphone and its associated electronics were designed and tested to record audio signals from 100 Hz to 10 kHz, a bandwidth that includes LIBS shock-waves but also natural

* Corresponding author.

E-mail address: baptiste.chide@isae-supaeo.fr (B. Chide).

atmospheric phenomena such as wind [8].

In LIBS, a short, focused laser pulse interacts with the target under high irradiance condition (irradiance $> 10 \text{ MW/mm}^2$) over a small area (a $300 \mu\text{m}$ to $500 \mu\text{m}$ spot in diameter for SuperCam) leading to material vaporization. The resulting plasma expands into the surrounding gas, faster than the speed of sound and generates a shock-wave [9]. Number of previous studies have proved that the LIBS shock-wave carries relevant information about the amount of laser energy absorbed by the target (laser-matter interaction) and about the plasma plume expansion. By recording the LIBS shock-wave, Conesa *et al.* [10] showed that the acoustic energy follows linearly the laser irradiance starting from low levels. A slope change for higher irradiances is also believed to indicate different plasma formation dynamics suggesting that the shock-wave recording is an efficient tool to monitor the plasma formation and evolution. It has also been proved that the conversion efficiency between incident laser beam and shock-wave energy can be estimated using a blast-wave theoretical model [11,12]. Therefore, the study of the LIBS shock-wave gives insight into the coupling between the laser and the matter. Krasniker *et al.* [13] further extended this relationship between laser-matter interaction and the shock-wave velocity to characterize the physical matrix effect of the targeted sample. More specifically, Abdel-Salam *et al.* [14] established a correlation between shock-wave velocity and hardness of calcified tissues. As the laser-matter interaction governs the ablation process, Stauter *et al.* [15] proposed a calibration curve that links the ablation rate on the surface with the shock-wave velocity for a given laser fluence. Furthermore, under some controlled conditions in the laboratory, Chen and Yeung [16], Hrdlička *et al.* [17] concluded that acoustic data provide a useful tool to normalize LIBS spectra as it can be used to correct LIBS emission lines from shot-to-shot fluctuations. It is a critical step for field applications where operational conditions can vary a lot.

Using multiple shots to penetrate into the sample allows a depth-profile analysis of the target composition. However, as a cavity forms, the characteristics of the laser-sample interactions change, modifying the pulse-to-pulse ablation rate [18]. Moreover, the confinement of the plasma within the cavity modifies its properties (temperature and electron density) with depth [19] and alters the LIBS emission signal [20]. The latter study also showed a modification of the shock-wave propagation geometry from a spherical front when the laser impact occurs on a surface, to a planar front when the laser impact occurs in a crater. This change of the acoustic signal with the depth was also seen by Grad and Možina [21] who used the acoustic energy as an indicator of the crater growth during a depth profile.

Very few publications attempt to correlate the acoustic signal of the laser-induced shock-wave during a depth profile with both the volume of the cavity and the LIBS emission spectra. Chaléard *et al.* [22] worked on a matrix effect correction method using the acoustic signal as a tracer of the ablated mass for several metallic targets in air at ambient pressure. Using a plasma temperature estimation and the acoustic signal as a normalization factor, this study presented a good correlation between the normalized copper line and the copper concentration ($R^2 = 0.9996$). The measurements were averaged over a series of 500 shots, but none of the following were analyzed: the shot-to-shot variations of the volume, the shot-to-shot variations of the acoustic signal and the shot-to-shot variations of emission lines' intensity. More recently, as part of the Mars Microphone test campaign, Murdoch *et al.* [8] characterized the behavior of the LIBS acoustic signal as a function of the number of laser shots in the same crater under a simulated Martian atmosphere at two different plasma-to-microphone distances. Although the decrease of the acoustic energy was attributed to the growth of the crater, its evolution was not monitored. Attempting to determine possible correlations between the acoustic signal and the plasma emission lines was not part of this experimental campaign either.

Our study compares for the first time the shot-to-shot evolution of the LIBS acoustic signal, the crater volume, and the line emission

intensities during LIBS depth-profile analysis on various geological targets. Although the application to SuperCam on Mars is the objective of the combined LIBS and microphone investigation, this initial study is conducted at ambient pressure to assess the relationships to be expected for these combined measurements. We propose a detailed diagnostic of the ablation process with the help of the LIBS shock-wave recording, and show to what extent acoustic measurements can add complementary information to LIBS analytical capabilities.

2. Experimental set-up

2.1. ChemCam replica

The LIBS capability of SuperCam is inherited from the ChemCam instrument onboard the Curiosity rover. To reproduce as closely as possible the instrument characteristics, the ChemCam Mast-Unit Engineering and Qualification Model is used in this study to ablate the targets analyzed with a 5 ns infrared laser pulse. The instrument is cooled to the laser' optimal operating temperature of -10°C to reach an energy deposited on the target of $\sim 10 \text{ mJ}$ which is of the same order of magnitude as the energy levels reached on Mars with ChemCam and expected for SuperCam. The LIBS spectra are collected at room temperature with the ChemCam Body-Unit Engineering Model. The spectrometers' detectors are not time-gated and the overall plasma spectral emission (including emission lines and continuum emission) is integrated over $\sim 10 \text{ ms}$ [23].

2.2. Acoustic test bench under Earth atmosphere

The ChemCam laser is fired inside a homemade anechoic box designed to shield the acoustic signal from the clean room environmental noise and to avoid uncontrolled resonance modes (see Fig. 1(b, c)). The double walls of this $78 \times 67 \times 88 \text{ cm}$ chamber are made of 22 mm thick medium-density fiberboard (750 kg/m^3) panels which are separated by a commercial extruded polystyrene sound insulator 15 mm thick. The inner walls are covered by a pyramidal acoustic foam of polyurethane used to reduce echoes and reverberations inside the test bench. The total height of the foam is 80 mm. The entire test bench is operated under ambient pressure and temperature.

The 1067 nm laser is directed onto a folding mirror that reflects the beam downward through a circular glass window that is mounted on the top of the chamber and is transparent to both the laser beam and plasma light. The analyzed targets are placed on a horizontal foam support at the bottom of the chamber to prevent sound transmission through the structure. Targets are impacted at 0° incident angle by the laser (see Fig. 1(b)). The optical path length between the laser and the targets varies from 1783 mm to 1808 mm depending on the height of the target and its position on the foam support.

The cover of the anechoic box is equipped with two microphones. First, a SuperCam Mars Microphone (Knowles Electret model EK-23132) from the same batch as the microphone flight model (see Fig. 1(a)) is used. It is connected to a power supply that delivers 3.3 V needed to power the integrated preamplifier. The microphone sensitivity is 22.4 mV/Pa and there is no additional stage of amplification. The second microphone is a calibrated Bruel & Kjaer 4138 $\frac{1}{8}$ inch microphone, negatively polarized and connected to a preamplifier. The sensitivity is 31.6 mV/Pa . The signals from the SuperCam and the reference microphones are acquired by a portable USB 16-bit oscilloscope (TiePie Handyscope HS4) at 200 kHz. The acquisition system allows continuous time series recordings with no limitation of duration. The two microphones are located on both sides of the window and point downwards to the middle of the sample support. The measured inclination between the incident laser beam and the line of sight of both microphones does not exceed 20° . The two microphones are located at $\sim 65 \text{ cm}$ from the samples.

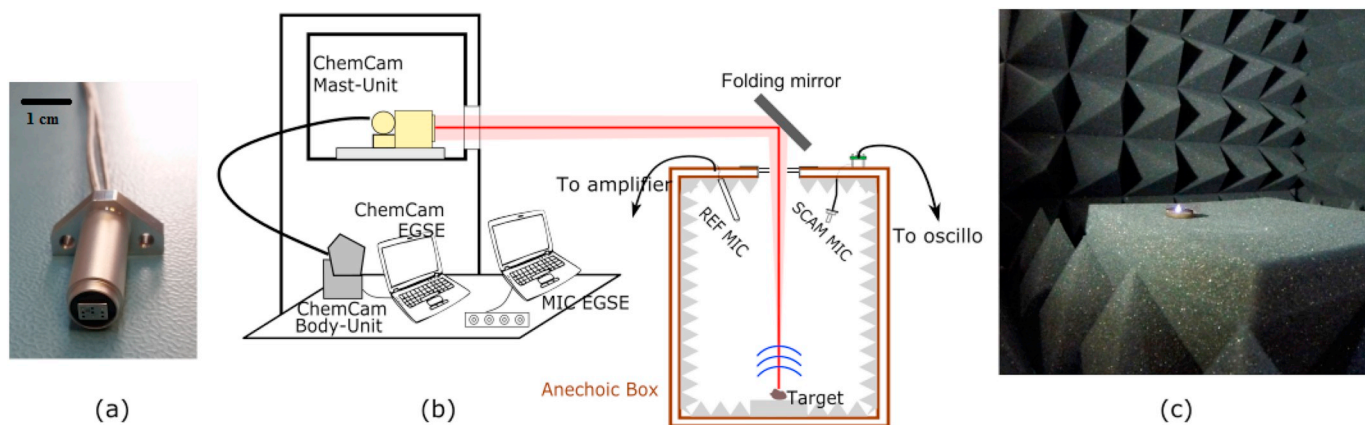


Fig. 1. (a) Photos of the Mars Microphone flight model. (b) Schematic of the test bench under Earth atmosphere, MIC: Microphone, SCAM: SuperCam, EGSE: Electrical Ground Support Equipment, REF: reference, oscillo: oscilloscope. (c) Photo illustrating a sample impacted by the ChemCam laser inside the anechoic box.

2.3. Sample preparation and experimental procedure

Eight homogeneous samples are prepared and selected to test the influence of basic rock properties with regards to LIBS acoustic signal. The number of targets is small on purpose, with the targets chosen to narrow the number of parameters influencing the laser-target coupling. Among them, three pressed pellets consisted of Johnson Space Center Mars 1 (JSC), a Martian soil simulant [24], sieved with a grain size smaller than 45 μm . These pellets are compacted with a load of 1 ton, 3 tons and 10 tons in order to reach an increasing level of hardness and density (see Fig. 2(a, b, c)). Two calcium-rich targets are also analyzed: a piece of solid calcium-sulfate plaster, referenced as gypsum hereafter, and a rectangular block of black marble (see Fig. 2(d, e)). The three remaining targets are iron-rich (see Fig. 2(f, g, h)): a piece of hematite, a piece of magnetite and a slice of the Chinga meteorite [25]. Hardness measurements were conducted with a Micro Vickers Hardness Tester (Buelher MVK H1) and a summary of the target physical properties is presented in Table 1. One can notice that the density varies the same way than hardness except for the meteorite which is the densest target but has an intermediate hardness.

The laser is fired at 3 Hz after an autofocus was performed in the center of each target. Then, we make series of LIBS pits with different total numbers of shots (5, 15, 30, 90, 150 and 300); each experimental condition is repeated 2 or 3 times depending on the target. LIBS craters obtained with different numbers of shots are annotated with colored

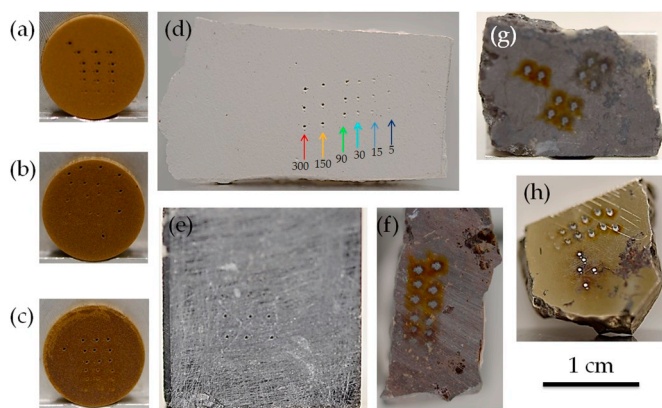


Fig. 2. Targets analyzed: (a) JSC-1 Mars simulant powder compacted by 1 ton of pressure, (b) JSC-1, 3 tons of pressure, (c) JSC-1, 10 tons of pressure, (d) gypsum, (e) black marble, (f) hematite, (g) magnetite and (h) Chinga (ataxite iron meteorite). The six craters resulting from an increasing number of shots are annotated with colored arrows for (d). The scale is the same for all the pictures.

Table 1

Summary of all the samples used in the experiment and their physical properties.

Target	Type	Density (g/cm^3)	Vickers Hardness
Gypsum	Plaster slice	1.0	3
JSC-1t	Pressed pellet	1.3	17
JSC-3t	Pressed pellet	1.7	29
JSC-10t	Pressed pellet	1.9	46
Black Marble	Rock sugar	2.69	177
Magnetite	Natural rock	4.75	767
Hematite	Natural rock	4.33	1014
Chinga meteorite	Slice	7.9	290

arrows in Fig. 2(d). For the JSC pellets and gypsum, all the craters are clearly visible and well defined. The roughness of the black marble makes shallower pits harder to see with a eye. For the iron-rich targets, a halo related to oxidation effects highlights the contours of the craters [26].

2.4. LIBS spectra processing and wavelength calibration

In parallel with sound recording, LIBS spectra are acquired for every laser shot. The ChemCam Body-Unit has three spectrometers collecting the plasma light emission over the UV (240.1 nm–342.2 nm), violet (382.1 nm–469.3 nm), and visible plus near infrared (474 nm–906 nm) ranges [3]. Each spectrum goes through a processing pipeline similar to the one presented in Wiens et al. [23]: subtracting the average passive reflectance spectrum of the target, de-noising, and removing the continuous baseline from Bremsstrahlung and recombination radiations. In

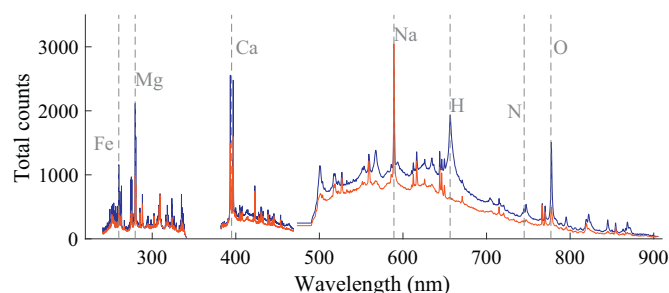


Fig. 3. Processed LIBS spectra with the continuum emission for the 1 ton compacted JSC target. The blue and red curves are respectively the first and the last spectrum over 300 consecutive shots on the same location. A few peaks are highlighted by dashed lines. (For interpretation of the references to colour in this figure legend, the reader is referred to the web version of this article.)

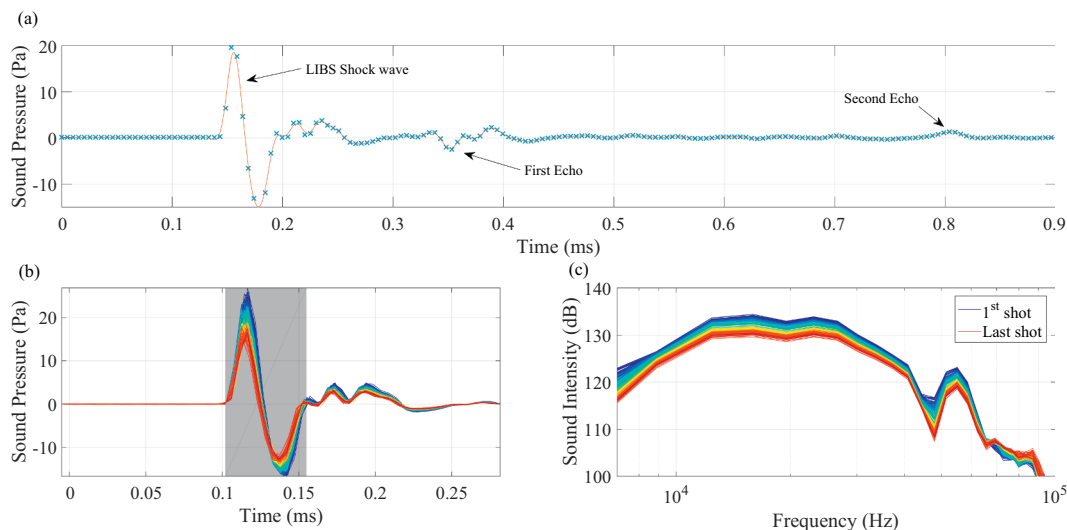


Fig. 4. Typical waveform of a LIBS shock-wave in ambient Earth atmosphere recorded by the SuperCam Microphone (a) on a 3 ton compacted JSC pellet (40th shot over a series of 150 shots). Blue crosses are experimental points interpolated by a smoothing spline (red curve). Evolution of the waveform (b) and acoustic spectrum (c) for a series of 150 consecutive shots on the same location recorded by the SuperCam Microphone. The shaded area represents the time window of integration for the acoustic energy computation. Colour code is the same for (b) and (c). (For interpretation of the references to colour in this figure legend, the reader is referred to the web version of this article.)

the case of ChemCam laboratory spectra, it is possible not to remove this baseline. The wavelength calibration is performed by comparison with reference spectra. Two spectra including the continuum emission, are shown in Fig. 3 for the 1 ton compacted JSC target.

3. Results

3.1. The shot-to-shot variation of the acoustic energy

Fig. 4(a) shows the time series LIBS spark waveform recorded by the SuperCam microphone. A rarefaction follows a compression which corresponds to the passage of the pressure wave through the membrane. Oscillations occurring after the rarefaction are attributed to the resonance modes of the membrane. For the SuperCam microphone, the first echo arrives 195 μ s after the initial peak, corresponding to an extra travel distance of \sim 6.6 cm assuming a sound speed of 340 m.s⁻¹. This reflection, linked to the microphone geometry, occurs on the aluminum trapezoidal base at the end of the 3.1 cm long microphone pole (see Fig. 1(a)). It does not interfere with the primary shock-wave signal and it is attenuated by 19 dB. The second echo, occurring 800 μ s after the initial peak, corresponds to a travel distance of 13.6 cm. It is a reflection on the upper wall of the anechoic box, just above the SuperCam microphone (see Fig. 1(b)) and is strongly attenuated (i.e. by 24 dB) due to the acoustic foam. It may also include a contribution of a reflection occurring on the glass window of the anechoic box. The signal-to-noise ratio is 54 dB for the SuperCam microphone and for the initial peak.

Fig. 4(b) shows the response of the SuperCam microphone for 150 consecutive laser shots on the same location on the 3 ton compacted JSC target and Fig. 4(c) displays their representation in the frequency domain. The duration of the compression and rarefaction waves is $52 \pm 2 \mu$ s and the signal is broadband, centered around 20–30 kHz which is similar to the characteristics of the waveform measured by Bolaños *et al.* [27]. The 150 waveforms and spectra are stable and reproducible shot-to-shot but they have a decreasing amplitude with the number of shots at the same location: the sound pressure level ranges from 122 dB re 20 μ Pa⁻¹ (corresponding to a peak amplitude of 26.8 Pa) for the first shot of the sequence to 117 dB re 20 μ Pa (corresponding to a

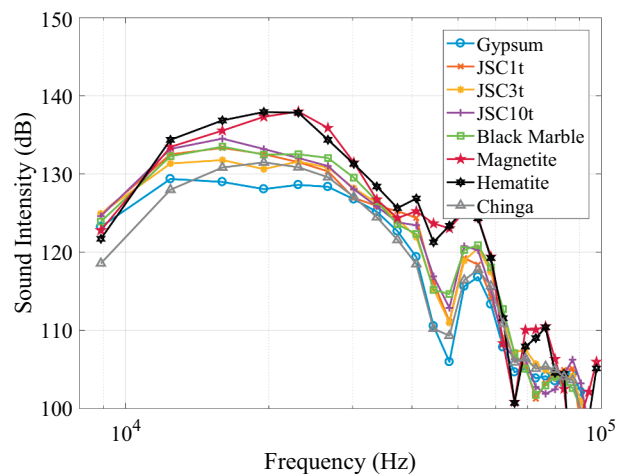


Fig. 5. Median spectra over a series of 150 shots for the 8 targets analyzed.

peak amplitude of 14.6 Pa) for the last shot. Other than the increased amplitude around 50–60 kHz (likely due to the microphone membrane resonance), no obvious spectral signatures are seen within the spectrum confirming that a shock-wave (a dirac pressure profile) is the source of the acoustic signal. Fig. 5 compares the median acoustic spectra for the eight targets analyzed. At this moderate frequency resolution resulting from the reduced time window delimited by the grey rectangle in Fig. 4(b), the spectra do not reveal any particular features and it seems that the nature of the target does not significantly influence the acoustic shape of these acoustic spectra.

Data from the SuperCam microphone and from the reference microphone (both in time and frequency domain) are compared in Fig. 6. It shows that the LIBS shock-wave signal recorded by the reference microphone results in a higher peak pressure amplitude and shorter pulse duration (leading to a higher frequency content). Moreover, the pressure front recorded by the reference microphone is sharper than the one observed by the SuperCam microphone. As it was already observed by Qin and Attenborough [28] with a $\frac{1}{8}$ inch and a $\frac{1}{4}$ inch microphone, this difference is essentially caused by the different bandwidth of the microphones. The SuperCam microphone (10 kHz cut-off frequency)

¹ $20 \log_{10} \left(\frac{P}{P_0} \right)$ with P the amplitude of the first peak in Pa and $P_0 = 20 \mu$ Pa, the reference sound pressure.

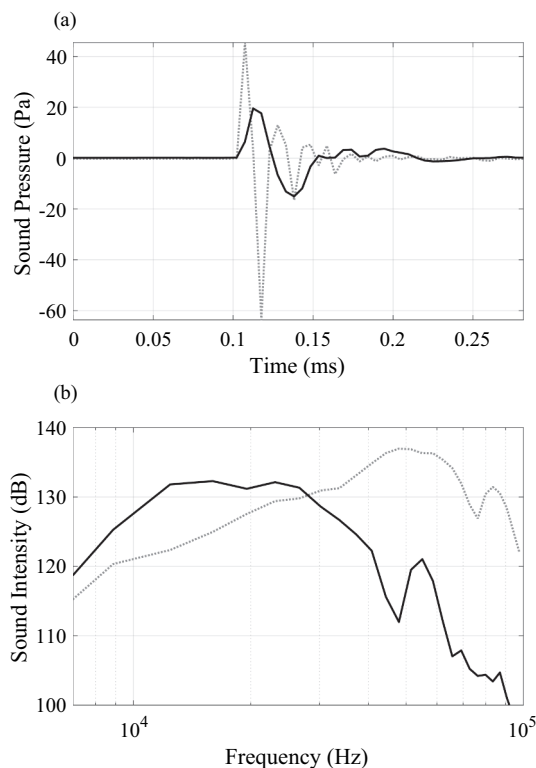


Fig. 6. Comparison between LIBS shock-wave recorded by the SuperCam microphone (black; solid line) and by the reference microphone (grey; dashed line) in the time domain (a) and in the frequency domain (b). Data correspond to the 40th shot over a series of 150 shots on the 3 ton compacted JSC target (same as Fig. 4(a)).

acts on the shock-wave signal as a stronger low-pass filter than the reference microphone (50 kHz cut-off frequency). Nevertheless, in the followings, only the SuperCam microphone results are reported since the reference microphone leads to the same conclusions.

To study the decrease in amplitude of the acoustic waveform as a function of the number of shots, the integral of the square values of the time series signal during the compression and rarefaction phases (hereafter named the acoustic energy) is computed for each single shot (see shaded area in Fig. 4(b) for the integration time window, e.g. Grad and Možina [21]). This parameter is found to follow the same trend as the peak-to-peak amplitude but with a smaller dispersion. Acoustic energy will therefore be used in this study to represent the acoustic signal. Fig. 7(a) shows the evolution of the acoustic energy during a series of 300 laser shots at the same location. For each target, the averaged 5 first acoustic energies range from $7 \times 10^4 \text{ Pa}^2$ to $3.1 \times 10^5 \text{ Pa}^2$. This acoustic energy value of the first shots, that mainly depends on the laser energy, is suspected to be related to target physical and chemical properties but also to the length of the optical path between the laser and the target (that is slightly different for each sample; see Section 2.3). However this relationship is not clear. Thus, as we are interested in the shot-to-shot variations, the acoustic energy is normalized to the average energy of the five first shots. The acoustic energy decreases exponentially with the number of laser shots for the gypsum, the JSC pellets and the black marble. For the hematite and magnetite it increases during the ten first shots and then decreases very slowly. For the hematite target, the acoustic energy decreases by 4% between its maximum value (near the 10th shot) and the 300th shot, whereas for the gypsum it decreases by 93% which corresponds to a sound pressure level loss of 0.2 dB re 20 μPa (1.1 Pa) and 17 dB re 20 μPa (14.6 Pa) respectively. For the Chinga meteorite, the acoustic energy is constant after an increase for the 30 first shots. Fig. 7(b, c) show the variation of

the exponential decay rate as a function of the density and hardness of the targets. The decay rate of the acoustic energy varies the same way than the target density: the lower the density of the target, the larger the slope. It also varies the same way than the target hardness, except for the Chinga meteorite which has an intermediate hardness and an almost constant acoustic energy along the ablation process. However, this single target is not enough to settle whether density or hardness influences the decay rate of the acoustic energy.

The results of this section confirm the trend observed acoustically in Murdoch *et al.* [8] and noted spectrally for gypsum and other targets in Wiens *et al.* [23], and extends it over a larger range of densities/hardnesses and samples. In the former acoustic study, this behavior is attributed to different rates of growth of the LIBS craters. In order to test this hypothesis, we measured the crater depth reached after an increasing number of laser shots.

3.2. LIBS crater morphology

The morphologies of each crater made on the targets are analyzed with a non-contact 3D surface profiler (Sensofar S-NEOX) using confocal scanning. The resolution is 1 μm along the longitudinal axis and 1.3 μm transversally. Fig. 8 shows three examples of contour lines of a typical LIBS crater produced with 300 consecutive laser shots on a 1 ton compacted JSC pellet (a), 10 ton compacted JSC pellet (b) and the black marble (c). The pits have a similar shape, with a diameter of $425 \pm 25 \mu\text{m}$, similar to measurements conducted on an aluminum plate by Maurice *et al.* [2]. The maximal depth reached ranges from 370 μm for the black marble to 750 μm for the 1 ton compacted JSC pellet. In the latter example the cavity is deeper than its diameter, meaning that less light is reflected to the detector of the profiler from the bottom of the crater. This leads to a poorly resolved morphology at maximal depth (Fig. 8(a)).

For each of the 18 craters created on these three targets, the mean depth profile is computed in order to visualize the evolution of the crater as a function of the number of shots. It is the result of an average of 18 profiles centered on the barycenter of the crater and equally spaced by angles of 10°. The mean profiles for craters made with 5, 15, 30, 90, 150 and 300 shots on the three former targets are represented in Fig. 8(d, e, f). These figures show that the shape and depth of 3 replicates made with the same number of shots and on the same target are very reproducible. The diameter of the crater does not change with depth and does not seem to be a simple function of the target hardness. After only 5 shots, the crater cross-section is already established and does not increase anymore (see Fig. 8(a, b, c)). The crater profile presents a flat floor during the first 30 shots and then, as the depth increases, the ablation occurs preferentially in the center leading to a more conical shape. This shape evolution can be explained by the Gaussian distribution of the laser beam and an irradiance level that falls below the ablation threshold when the crater walls become too steep (see calculation details in Appendix A). It is worth noticing that the ablation rate decreases as the number of shots increases: for the 10 ton compacted JSC target, the laser ablated 420 μm depth during the first 150 shots whereas it ablated only 100 μm depth during the last 150 shots. Moreover, the ablation is more efficient on softer targets: after 300 shots the crater is twice as deep for the 1 ton compacted JSC pellet as for the black marble target (see Fig. 9).

The evolution of the volume of LIBS craters as a function of the number of shots is shown in Fig. 9(a). Data from the Chinga is missing because craters present an irregular and rough floor made of melted metal with a depth barely lower than 4 μm for the deepest pit. For the magnetite target, only craters resulting from 90, 150 and 300 laser shots are measured as it was not possible to precisely localize the contours of shallower pits resulting from 5, 15 and 30 laser shots. For each target, the solid line represents the function that best fits all the measured volumes. This figure confirms that the softer the target, the deeper the laser penetrates into the target. This target dependent

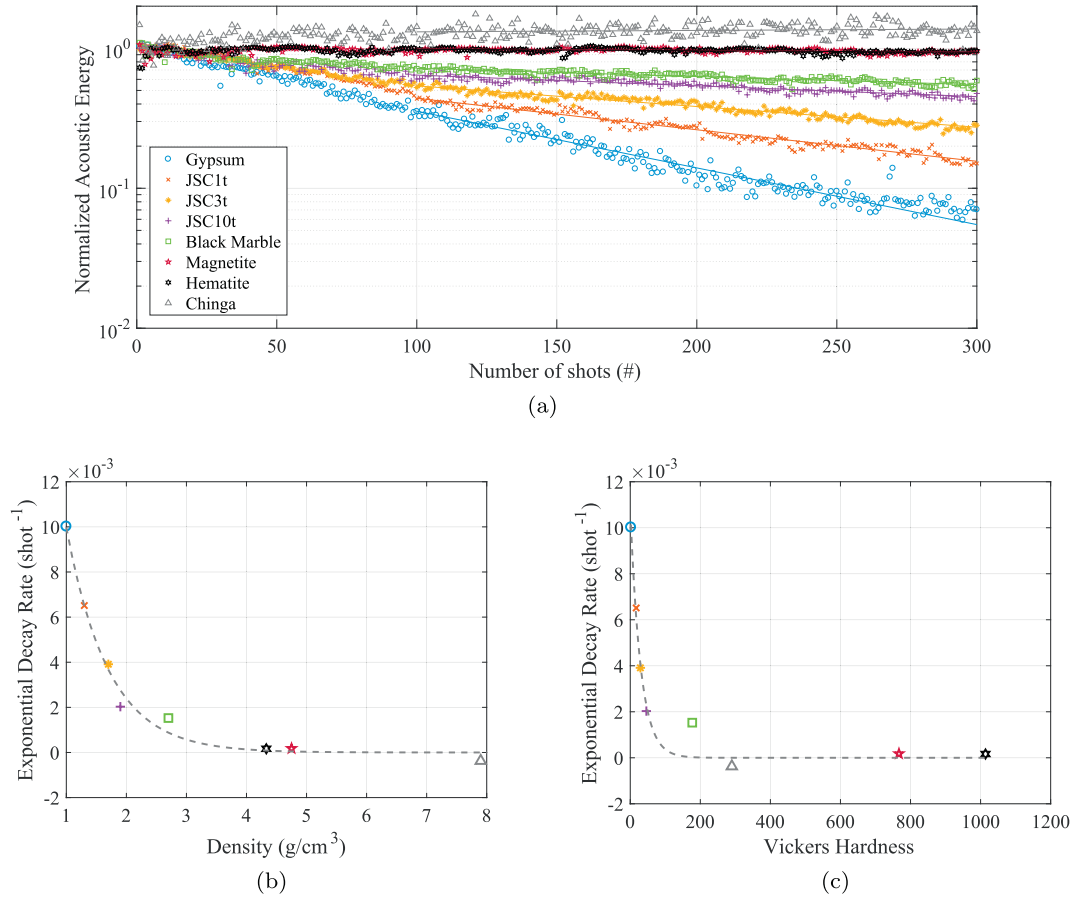


Fig. 7. (a) Variation of the acoustic energy during a series of 300 consecutive shots at the same location for the 8 analyzed targets. Each data set is the average over the 3 (or 2) series of 300 shots repeated over the same target. Each data set is fitted by a decreasing exponential function Ae^{-Bx} with B the exponential decay constant (solid line). (b) Exponential decay constant of the acoustic energy as a function of the density of the target and (c) as a function of the target hardness. Dotted grey lines are best fits with an exponential function.

ablated volume was already mentioned in Sallé *et al.* [29], as part of an experiment conducted under Mars atmosphere, where a laser was fired on basalt samples and metallic samples. This behavior was attributed to physical matrix effects but the denser the target was, the smaller the ablated volume. The evolution of the volume as a function of the number of shots is best fitted with a function of the form $y = a \ln x + bx + c$. As it was inferred from Fig. 8(d, e, f), the ablation rate drastically decreases during the first 50 shots and then the volume increases linearly: the ablation rate seems to converge to a constant value, at least within the 300 shots limit that was investigated. This phase of high ablation followed by a low and stable penetration rate after about a hundred of shots was previously noticed in Maurice *et al.* [5] under Mars atmosphere. It is believed that this decrease comes from a complex loss of coupling between the laser and the crater walls (see Appendix A). More factors, including changes in plasma properties also contribute to this decrease and are discussed in Section 4.

3.3. Acoustic measurements to trace the ablation process

It is impossible to directly measure the depth of the laser pits produced by LIBS on Mars. This knowledge would be valuable as it would help to decipher a variation of the LIBS signal showing changes in plasma parameters due to chemical target stratification with depth, as encountered during a depth profile [e.g. 30,31]. Fig. 10 synthesizes results presented in previous sections as a relationship between the acoustic energy and the crater volume; for a given crater, it links the volume of the crater with the acoustic energy of the last shot of the raster that produced the crater. Red points resulting from 300 shots at

the same location reveal deeper craters when the target is softer. A clear linear decrease of the acoustic energy with crater volume can be noticed. One remarkable feature is that this decrease appears to be independent of the target hardness or density. This relationship means that the recording of the acoustic energy can be used to monitor the LIBS crater volume reached after a given number of shots. For instance, if the acoustic energy decreases by 60% (i.e., a normalized acoustic energy of 0.4), the ablated volume is $3 \times 10^7 \pm 0.5 \times 10^7 \mu\text{m}^3$. For the deepest crater, a large dispersion in the volume measurement is indicative of the difficult crater characterization conditions: the sound is low and a deep crater with steep walls is close to the profiler measurement limitations. To explain this linear trend, it can be inferred that a shock-wave generated deeper results from a downgraded laser-matter interaction compared with laser-surface interaction. Therefore, less energy is locally deposited on the target, leading to less vaporized mass [32]. Simultaneously, less energy is released in the blast resulting in a less energetic shock front [33]. This loss of normalized energy with depth is assumed to be, to first order, unrelated to target physical properties. As a consequence, we conclude that the acoustic data recorded by the microphone can be used as a proxy of the total ablated volume of material for all of the LIBS targets.

4. Discussion

The acoustic behavior during a depth profile is also compared with the shot-to-shot variation of the LIBS spectrum. The total LIBS spectrum intensity and the acoustic energy as a function of the number of shots are represented in Fig. 11 for the eight analyzed targets. Two different

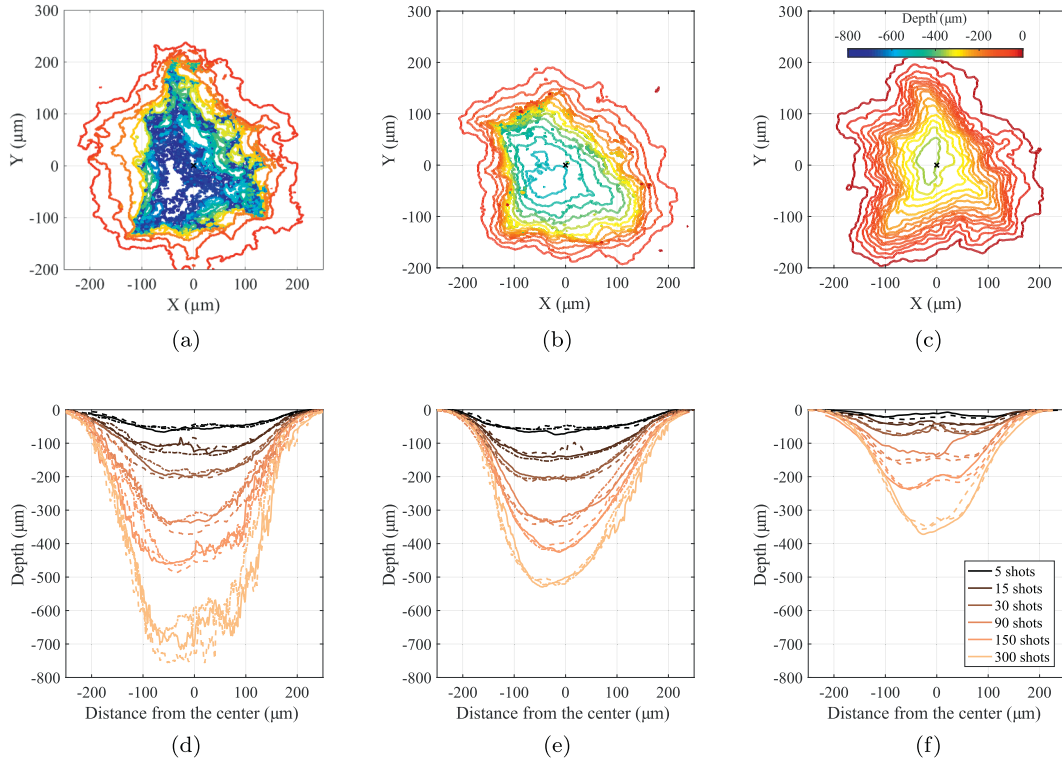


Fig. 8. Iso-depth lines for craters ablated with 300 consecutive laser shots onto 1 ton compacted JSC (a), 10 ton compacted JSC (b), and black marble (c). The black crosses symbolize the geometric center of the pits. Mean profiles of the 18 craters ablated in the 1 ton compacted JSC pellet (d), in the 10 ton compacted JSC target (e) and in the black marble (f). The solid, dotted and dashed lines in (d)–(f) correspond to the 3 occurrences of the craters ablated with the same number of shots.

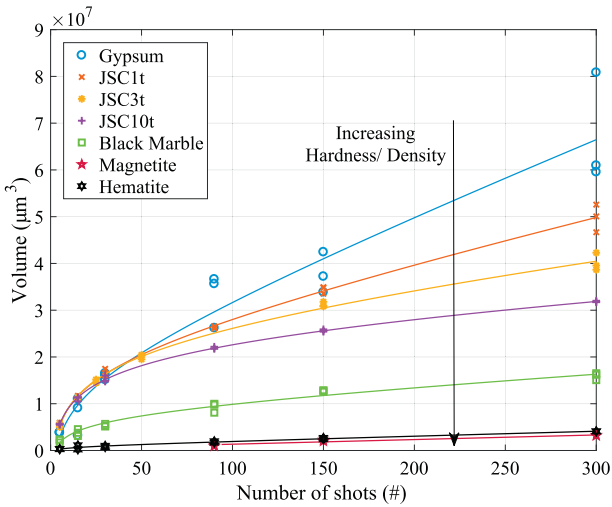


Fig. 9. Evolution of the ablated volume as a function of the number of laser shots deposited in the crater. The solid line corresponds to the function that best fits all the measured points per target using a linear function for the magnetite (no data below 90 shots, see text for details) and $f(x) = a \ln x + bx + c$ for the six other targets.

behaviors can be discussed. First, for the denser targets (magnetite, hematite and Chinga) the LIBS signal follows the same variation as the acoustic energy. Because the resulting cavity is shallow (ablated volume $< 5 \times 10^6 \mu\text{m}^3$ for 300 shots), the change of acoustic energy is relatively low: as the depth-to-diameter ratios of these craters is small, there is no confinement effect that cause modifications of the plasma properties. However, for the five other targets, where the laser

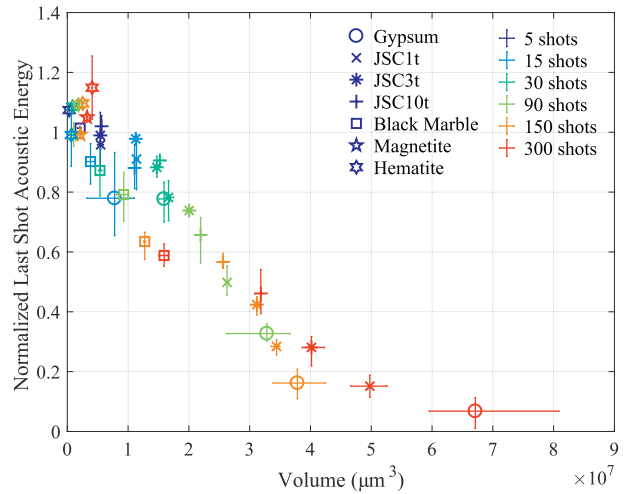


Fig. 10. Normalized acoustic energy at the bottom of the crater (i.e. last shot acoustic energy) as a function of the cavity volume. Error bars are computed using the 2 or 3 replicate craters with the same number of shots. The colour code represents the number of shots that created the craters.

penetrates much more (see Fig. 9(a)), the LIBS spectrum intensity and acoustic energy are not correlated. For the gypsum, the LIBS spectrum intensity is constant during the 70 first shots and then decreases with the number of shots. For the 1 ton compacted JSC, a rapid increase of the LIBS signal is followed by a constant phase then the LIBS spectrum intensity decreases. The same behavior is observed for the 3 ton compacted JSC except that the initial increase occurs over the 60 first shots

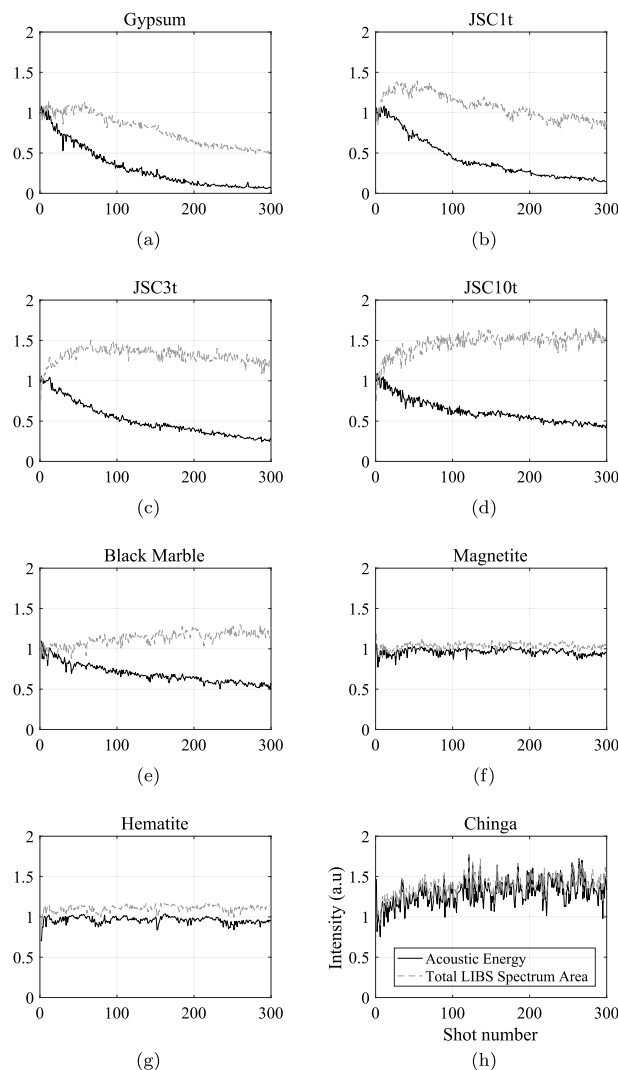


Fig. 11. Variation of the acoustic energy (black) and the LIBS signal (spectrum area; grey) as a function of the number of shots for the 8 analyzed targets.

compared to the 20 first shots for the 1 ton compacted JSC. The decrease after ~ 100 shots is lower than in the 1 ton compacted JSC. For the 10 ton compacted JSC, the LIBS spectrum intensity increases during the first ~ 100 shots and then stays constant. Lastly, for the black marble, only the starting increasing phase is seen. This non monotonic behavior of the LIBS signal is not directly linked with the acoustic energy and could be attributed to a cavity effect that induces different plasma formation conditions. Corsi et al. [20] explains that a plasma confined in a crater is hotter and denser, and consequently presents an enhanced LIBS signal intensity. As the crater grows, this effect competes with the cooling of the plasma by interaction with the crater walls leading to a decrease of the plasma temperature and thus the LIBS emission. Moreover, as the plasma confined inside a crater is denser, the inverse Bremsstrahlung effect shields the plasma and reduces the laser energy deposited on the target. This effect reduces the ablation rate and also tends to reduce the LIBS emission. To a lesser extent, the steep angles of the crater walls reduce the laser-mater coupling as described in Appendix A. But on the other hand, at these higher local incidence angles, a fraction of the laser beam that reaches the crater wall might be redistributed inside the crater due to multiple reflections

in the crater walls [34]. Then the beam would remain active for further interaction inside the crater. For the five softer targets, the LIBS spectra area evolution is assumed to be governed by these competing effects but a detailed investigation is out of the scope of this study. Nevertheless, the acoustic energy seems to be well correlated with the ablation and less impacted by changes in plasma properties than the LIBS optical signal that is very sensitive to changes in plasma temperature and electron density under terrestrial atmosphere. In the end, results presented in Section 3.1 showed that the acoustic energy gives an information about the ablation that is independent from the information contained in the LIBS spectrum.

5. Conclusion

As part of the SuperCam/Mars2020 microphone investigation, a detailed study of the relationship between the LIBS acoustic signal, ablated volume and LIBS emission spectrum is performed at ambient pressure on eight different geological samples with varying chemical and physical properties of interest.

Recording the acoustic signal of the LIBS shock-wave shows that

only the amplitude of the signal decreases as a function of the number of shots during a depth profile, while the acoustic waveform remains the same. This decrease is steeper for softer/less dense targets and the exponential decay rate of the acoustic energy is controlled by target hardness and density.

The measurement of crater morphology after a given number of shots in the same location reveals that the crater shape and depth is quite reproducible for the same target and the same number of shots. However, the penetration depth depends on the target hardness/density: the softer the target is, the deeper the laser ablates it. The evolution of the crater volume as a function of the number of shots shows that the ablation rate decreases drastically during a depth profile because of a decrease in laser-matter interaction. Our experiments also exhibit a linear relationship between the normalized acoustic energy and the ablated volume. It demonstrates that the acoustic energy can be used as a tool to monitor the ablated volume regardless of the physical properties of the target, a piece of information not provided by the analysis of the LIBS spectra. This demonstrates that the Mars Microphone will add valuable new data to study of the thicknesses of coatings and alteration layers with the LIBS capability of SuperCam.

Appendix A. Laser irradiance over the walls of LIBS craters

To explain the evolution of the shape of the crater with increasing numbers of pulses as it is impacted by the laser, we model very simply how the laser energy is distributed over the crater walls and floor. On a planar surface normal to the laser beam, the spatial irradiance distribution of the ChemCam qualification model laser can be approximated as a Gaussian distribution:

$$I(r) = I_0 e^{-\frac{2r^2}{w_0^2}} \quad (\text{A.1})$$

where $I(r)$ is the irradiance at a distance r from the center of the spot, I_0 the maximal amplitude of 65 MW/mm^2 for a target at $\sim 1.8 \text{ m}$ from the instrument and $w_0 = 240 \text{ }\mu\text{m}$ the characteristic length. All these values are extracted from Rapin [35]. The irradiance threshold to ablate material is of the order of 10 MW/mm^2 . This simulated laser irradiance profile is represented in Fig. A.12.

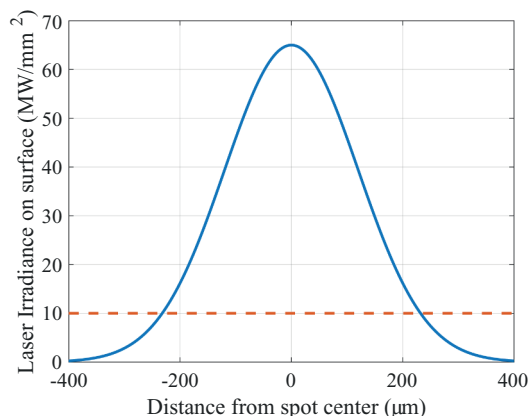


Fig. A.12. Simplified laser irradiance profile for a planar target surface perpendicular to the laser beam at a distance of 1.8 from the laser (blue curve) and approximate irradiance ablation threshold (red dashed line). This Gaussian distribution was simulated using data from Rapin [35] (see in text). (For interpretation of the references to colour in this figure legend, the reader is referred to the web version of this article.)

When a crater forms, the laser beam no longer impacts the surface with an angle of 90° but with an angle that depends on the slope of each single point inside the crater. Therefore, laser power locally deposited on a crater wall is reduced by a factor $\cos\alpha$ compared with a normal surface, with α being the local angle between the horizontal and the crater wall. Fig. A.13 shows a crater profile resulting from 90 shots in the 10 ton compacted JSC target and its associated attenuation factor. It shows that the interaction reduces significantly over the inclined walls of the crater and is at its maximum on the crater floor which is orthogonal to the laser beam. Multiplying this attenuation factor by the laser irradiance profile gives the level of irradiance reached at each point of the crater. These levels are represented in Fig. A.14 for six craters, with increasing depth, created on the 10 ton compacted JSC target. It shows that the irradiance level is far above the ablation threshold at the bottom of the crater and decreases on the walls which confirms that the laser ablates preferentially in the center of the pit. For the two first craters, resulting from 5 and 15 shots respectively, the irradiance does not fall below the ablation threshold and the material is vaporized over the entire spot area. Starting with 30 shots, parts of the crater wall fall below the ablation threshold (see black points in Fig. A.14). However, the two deepest craters show that portions of the crater wall that are nominally below this threshold are nonetheless ablated. It can also be noted that the threshold value of 10 MW/mm^2 is dependent on the material but there could be other phenomena at work here, such as erosion or possibly sputtering by material being ejected from the hole.

Lastly, the acoustic energy is confirmed to be a reliable indicator of the ablation, and provides a complementary information that can not be derived from the analysis of the LIBS spectrum.

These initial results using acoustics to infer target hardness and LIBS crater volume are promising and show the potential of acoustic data for LIBS investigations on Mars and elsewhere. Future work will consolidate these findings by quantifying the influence of target physical properties on acoustic energy with a more exhaustive set of representative geological samples. As the goal is to operate the microphone on the surface of Mars, this study is currently extended to determine the applicability of these conclusions to LIBS at Martian atmospheric pressure.

Acknowledgments

This work was funded by CNES and Région Occitanie as part of a PhD thesis. We gratefully acknowledge Guy Perez from CNES for his help with the 3D-surface profiler. The NASA Mars Exploration Program supported some parts (ChemCam body unit, RCW participation).

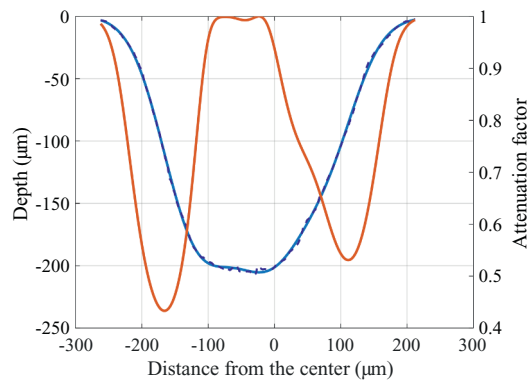


Fig. A.13. Profile of a crater resulting from 90 shots in the 10 ton compacted JSC target (blue curve). The dashed line corresponds to the data presented in Fig. 8(e) and the solid line to the function that best fits the crater profile (a sum of two Gaussian functions). The local angles of the crater (angles against the normal of the crater walls) were computed using the derivative of this fitted function. The red curve symbolizes angle-induced laser beam attenuation factor, computed as the cosine of the local angle. (For interpretation of the references to colour in this figure legend, the reader is referred to the web version of this article.)

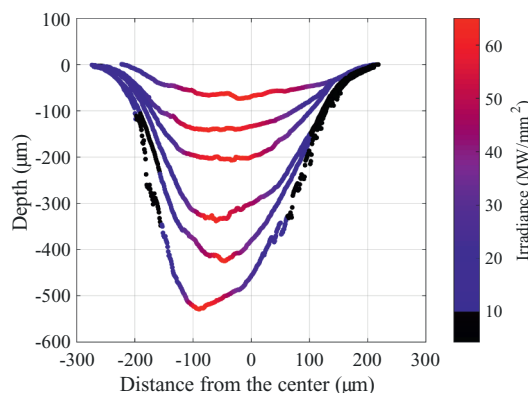


Fig. A.14. Computed laser irradiance over craters resulting from 5, 15, 30, 90, 150 and 300 shots on the 10 ton compacted JSC target. Black points present an irradiance level below the nominal ablation threshold of 10 MW/mm².

References

- [1] D.A. Cremers, F.-Y. Yueh, J.P. Singh, H. Zhang, Laser-Induced Breakdown Spectroscopy, Elemental Analysis, American Cancer Society, 2012, <https://doi.org/10.1002/9780470027318.a0708.pub2>.
- [2] S. Maurice, R.C. Wiens, M. Saccoccio, B. Barraclough, O. Gasnault, O. Forni, N. Mangold, D. Baratoux, S. Bender, G. Berger, J. Bernardin, M. Berthé, N. Bridges, D. Blaney, M. Bouyé, P. Cais, B. Clark, S. Clegg, A. Cousin, D. Cremers, A. Cros, L. DeFlores, C. Derycke, B. Dingler, G. Dromart, B. Dubois, M. Dupieux, E. Durand, L. d'Uston, C. Fabre, B. Faure, A. Gaboriaud, T. Gharsa, K. Herkenhoff, E. Kan, L. Kirkland, D. Kouach, J.-L. Lacour, Y. Langevin, J. Lasue, S. Le Mouélic, M. Lescure, E. Lewin, D. Limonadi, G. Manhès, P. Mauchien, C. McKay, P.-Y. Meslin, Y. Michel, E. Miller, H.E. Newsom, G. Orttner, A. Paillet, L. Parès, Y. Parot, R. Pérez, P. Pinet, F. Poitrasson, B. Quertier, B. Sallé, C. Sotin, V. Sautter, H. Séran, J.J. Simmonds, J.-B. Sirven, R. Stiglich, N. Striebig, J.-J. Thocaven, M.J. Toplis, D. Vaniman, The chemcam instrument suite on the mars science laboratory (msl) rover: science objectives and mast unit description, *Space Sci. Rev.* 170 (2012) 95–166, <https://doi.org/10.1007/s11214-012-9912-2>.
- [3] R.C. Wiens, S. Maurice, B. Barraclough, M. Saccoccio, W.C. Barkley, J.F. Bell, S. Bender, J. Bernardin, D. Blaney, J. Blank, M. Bouyé, N. Bridges, N. Bultman, P. Cañs, R.C. Clanton, B. Clark, S. Clegg, A. Cousin, D. Cremers, A. Cros, L. DeFlores, D. Delapp, R. Dingler, C. D'Uston, M.D. Dyar, T. Elliott, D. Enemark, C. Fabre, M. Flores, O. Forni, O. Gasnault, T. Hale, C. Hays, K. Herkenhoff, E. Kan, L. Kirkland, D. Kouach, D. Landis, Y. Langevin, N. Lanza, F. LaRocca, J. Lasue, J. Latino, D. Limonadi, C. Lindensmith, C. Little, N. Mangold, G. Manhès, P. Mauchien, C. McKay, E. Miller, J. Mooney, R.V. Morris, L. Morrison, T. Nelson, H. Newsom, A. Ollila, M. Ott, L. Pares, R. Perez, F. Poitrasson, C. Provost, J.W. Reiter, T. Roberts, F. Romero, V. Sautter, S. Salazar, J.J. Simmonds, R. Stiglich, S. Storms, N. Striebig, J.-J. Thocaven, T. Trujillo, M. Ulibarri, D. Vaniman, N. Warner, R. Waterbury, R. Whitaker, J. Witt, B. Wong-Swanson, The ChemCam instrument suite on the mars science laboratory (MSL) rover: body unit and combined system tests, *Space Sci. Rev.* 170 (2012) 167–227, <https://doi.org/10.1007/s11214-012-9902-4>.
- [4] R.C. Wiens, S. Maurice, ChemCam: chemostratigraphy by the first mars microprobe, *Elements* 11 (2015) 33–38, <https://doi.org/10.2113/gselements.11.1.33>.
- [5] S. Maurice, S.M. Clegg, R.C. Wiens, O. Gasnault, W. Rapin, O. Forni, A. Cousin, V. Sautter, N. Mangold, L.L. Deit, M. Nachon, R.B. Anderson, N.L. Lanza, C. Fabre, V. Payré, J. Lasue, P.-Y. Meslin, R.J. Léveillé, B.L. Barraclough, P. Beck, S.C. Bender, G. Berger, J.C. Bridges, N.T. Bridges, G. Dromart, M.D. Dyar, R. Francis, J. Frydenvang, B. Gondet, B.L. Ehlmann, K.E. Herkenhoff, J.R. Johnson, Y. Langevin, M.B. Madsen, N. Melikechi, J.-L. Lacour, S.L. Mouélic, E. Lewin, H.E. Newsom, A.M. Ollila, P. Pinet, S. Schröder, J.-B. Sirven, R.L. Tokar, M.J. Toplis, C. d'Uston, D.T. Vaniman, A.R. Vasavada, ChemCam activities and discoveries during the nominal mission of the mars science laboratory in gale crater, *mars, J. Anal. Atom. Spectrom.* 31 (2016) 863–889, <https://doi.org/10.1039/c5ja00417a>.
- [6] R.C. Wiens, S. Maurice, F.R. Perez, The supercam remote sensing instrument suite for the mars 2020 rover mission: a preview, *Spectroscopy* 32 (2017) 50–55 URL <http://www.spectroscopyonline.com/supercam-remote-sensing-instrument-suite-mars-2020-rover-preview>.
- [7] S. Maurice, R.C. Wiens, W. Rapin, D. Mimoun, X. Jacob, B. Betts, S. Clegg, A. Cousin, O. Gasnault, O. Forni, J. Lasue, P.-Y. Meslin, J.F. Bell, G. Delory, A microphone supporting LIBS investigation on mars, 47th Lunar and Planetary Science Conference, The Woodlands, TX, United States, 2016, p. 3044.
- [8] N. Murdoch, B. Chide, J. Lasue, A. Cadu, A. Sournac, M. Bassas-Portús, X. Jacob, J. Merrison, J. Iversen, C. Moretto, C. Velasco, L. Parès, A. Hynes, V. Godiver, R. Lorenz, P. Cais, P. Bernadi, S. Maurice, R. Wiens, D. Mimoun, Laser-induced breakdown spectroscopy acoustic testing of the mars 2020 microphone, *Planet. Space Sci.* 165 (2019) 260–271, <https://doi.org/10.1016/j.pss.2018.09.009>.
- [9] J.C. Miller (Ed.), Laser Ablation, Springer, Berlin, Heidelberg, 1994, <https://doi.org/10.1007/978-3-642-78720-1>.
- [10] S. Conesa, S. Palanco, J. Laserna, Acoustic and optical emission during laser-induced plasma formation, *Spectrochim. Acta B At. Spectrosc.* 59 (2004) 1395–1401, <https://doi.org/10.1016/j.sab.2004.06.004>.
- [11] J. Diaci, J. Možina, Investigation of blast waves generated by laser induced damage processes, *Opt. Commun.* 90 (1992) 73–78, [https://doi.org/10.1016/0030-4018\(92\)90331-K](https://doi.org/10.1016/0030-4018(92)90331-K).
- [12] S.H. Jeong, R. Greif, R.E. Russo, Shock wave and material vapour plume propagation during excimer laser ablation of aluminium samples, *J. Phys. D. Appl. Phys.* 32 (1999) 2578.

- [13] R. Krasniker, V. Bulatov, I. Schechter, Study of matrix effects in laser plasma spectroscopy by shock wave propagation, *Spectrochim. Acta B At. Spectrosc.* 56 (2001) 609–618, [https://doi.org/10.1016/S0584-8547\(01\)00194-X](https://doi.org/10.1016/S0584-8547(01)00194-X).
- [14] Z. Abdel-Salam, A. Galmed, E. Tognoni, M. Harith, Estimation of calcified tissues hardness via calcium and magnesium ionic to atomic line intensity ratio in laser induced breakdown spectra, *Spectrochim. Acta B At. Spectrosc.* 62 (2007) 1343–1347, <https://doi.org/10.1016/j.sab.2007.10.033>.
- [15] C. Stauter, P. Gérard, J. Fontaine, T. Engel, Laser ablation acoustical monitoring, *Appl. Surf. Sci.* 109–110 (1997) 174–178, [https://doi.org/10.1016/S0169-4332\(96\)00655-1](https://doi.org/10.1016/S0169-4332(96)00655-1).
- [16] G. Chen, E.S. Yeung, Acoustic signal as an internal standard for quantitation in laser-generated plumes, *Anal. Chem.* 60 (1988) 2258–2263, <https://doi.org/10.1021/ac00171a020>.
- [17] A. Hrdlička, L. Zaorálková, M. Galiová, T. Čtvrtníčková, V. Kanický, V. Otruba, K. Novotný, P. Krásenský, J. Kaiser, R. Malina, K. Pálenková, Correlation of acoustic and optical emission signals produced at 1064 and 532 nm laser-induced breakdown spectroscopy (LIBS) of glazed wall tiles, *Spectrochim. Acta B At. Spectrosc.* 64 (2009) 74–78, <https://doi.org/10.1016/j.sab.2008.10.043>.
- [18] M.A. Shannon, A simplified cavity analysis for estimating energy coupling during laser ablation and drilling of solids – theory, *Appl. Surf. Sci.* 127–129 (1998) 218–225, [https://doi.org/10.1016/S0169-4332\(97\)00635-1](https://doi.org/10.1016/S0169-4332(97)00635-1).
- [19] X. Zeng, X. Mao, S.S. Mao, J.H. Yoo, R. Greif, R.E. Russo, Laser–plasma interactions in fused silica cavities, *J. Appl. Phys.* 95 (2004) 816–822, <https://doi.org/10.1063/1.1635990>.
- [20] M. Corsi, G. Cristoforetti, M. Hidalgo, D. Iriarte, S. Legnaioli, V. Palleschi, A. Salvetti, E. Tognoni, Effect of laser-induced crater depth in laser-induced breakdown spectroscopy emission features, *Appl. Spectrosc.* 59 (2005) 853–860, <https://doi.org/10.1366/0003702054411607>.
- [21] L. Grad, J. Možina, Acoustic in situ monitoring of excimer laser ablation of different ceramics, *Appl. Surf. Sci.* 69 (1993) 370–375, [https://doi.org/10.1016/0169-4332\(93\)90536-k](https://doi.org/10.1016/0169-4332(93)90536-k).
- [22] C. Chaléard, P. Mauchien, N. Andre, J. Uebbing, J.L. Lacour, C. Geertsen, Correction of matrix effects in quantitative elemental analysis with laser ablation optical emission spectrometry, *J. Anal. At. Spectrom.* 12 (1997) 183–188, <https://doi.org/10.1039/a604456e>.
- [23] R.C. Wiens, S. Maurice, J. Lasue, O. Forni, R. Anderson, S. Clegg, S. Bender, D. Blaney, B. Barraclough, A. Cousin, L. Deflores, D. Delapp, M. Dyar, C. Fabre, O. Gasnault, N. Lanza, J. Mazoyer, N. Melikechi, P.-Y. Meslin, H. Newsom, A. Ollila, R. Perez, R. Tokar, D. Vaniman, Pre-flight calibration and initial data processing for the ChemCam laser-induced breakdown spectroscopy instrument on the mars science laboratory rover, *Spectrochim. Acta Part B Atom. Spectrosc.* 82 (2013) 1–27, <https://doi.org/10.1016/j.sab.2013.02.003>.
- [24] C.C. Allen, K.M. Jager, R.V. Morris, D.J. Lindstrom, M.M. Lindstrom, J.P. Lockwood, JSC MARS-1: a martian soil simulant, Space 98, American Society of Civil Engineers, 1998, [https://doi.org/10.1061/40339\(206\)54](https://doi.org/10.1061/40339(206)54).
- [25] V. Buchwald, Handbook of Iron Meteorites: Their History, Distribution, Composition and Structure. Iron meteorites Chinga Chupaderos, 2, University of California Press, 1975 URL <http://hdl.handle.net/10524/35670>.
- [26] A. Fau, O. Beyssac, K. Benzerara, S. Bernard, P.-Y. Meslin, A. Cousin, J. Boulliard, M. Gauthier, J. Manrique, S. Maurice, P.-Y. Meslin, G. Montagnac, R. Wiens, S. Maurice, O. Gasnault, Effect of LIBS laser shots on mineral structure and RAMAN signature: preparing for Mars2020 SuperCam instrument, 49th Lunar and Planetary Science Conference, The Woodlands, TX, United States, 2018, p. 2064.
- [27] J.G. Bolaños, V. Pulkki, P. Karppinen, E. Hæggröm, An optoacoustic point source for acoustic scale model measurements, *J. Acoust. Soc. Am.* 133 (2013) EL221–EL227, <https://doi.org/10.1121/1.4793566>.
- [28] Q. Qin, K. Attenborough, Characteristics and application of laser-generated acoustic shock waves in air, *Appl. Acoust.* 65 (2004) 325–340, <https://doi.org/10.1016/j.apacoust.2003.11.003>.
- [29] B. Sallé, J.-L. Lacour, E. Vors, P. Fichet, S. Maurice, D.A. Cremers, R.C. Wiens, Laser-induced breakdown spectroscopy for mars surface analysis: capabilities at stand-off distances and detection of chlorine and sulfur elements, *Spectrochim. Acta B At. Spectrosc.* 59 (2004) 1413–1422, <https://doi.org/10.1016/j.sab.2004.06.006>.
- [30] N.L. Lanza, A.M. Ollila, A. Cousin, R.C. Wiens, S. Clegg, N. Mangold, N. Bridges, D. Cooper, M. Schmidt, J. Berger, R. Arvidson, N. Melikechi, H.E. Newsom, R. Tokar, C. Hardgrove, A. Mezzacappa, R.S. Jackson, B. Clark, O. Forni, S. Maurice, M. Nachon, R.B. Anderson, J. Blank, M. Deans, D. Delapp, R. Lévillé, R. McInroy, R. Martinez, P.-Y. Meslin, P. Pinet, Understanding the signature of rock coatings in laser-induced breakdown spectroscopy data, *Icarus* 249 (2015) 62–73, <https://doi.org/10.1016/j.icarus.2014.05.038>.
- [31] N.L. Lanza, R.C. Wiens, R.E. Arvidson, B.C. Clark, W.W. Fischer, R. Gellert, J.P. Grotzinger, J.A. Hurowitz, S.M. McLennan, R.V. Morris, M.S. Rice, J.F. Bell, J.A. Berger, D.L. Blaney, N.T. Bridges, F. Calef, J.L. Campbell, S.M. Clegg, A. Cousin, K.S. Edgett, C. Fabre, M.R. Fisk, O. Forni, J. Frydenvang, K.R. Hardy, C. Hardgrove, J.R. Johnson, J. Lasue, S.L. Mouélic, M.C. Malin, N. Mangold, J. Martn-Torres, S. Maurice, M.J. McBride, D.W. Ming, H.E. Newsom, A.M. Ollila, V. Sautter, S. Schröder, L.M. Thompson, A.H. Treiman, S. VanBommel, D.T. Vaniman, M.-P. Zorzano, Oxidation of manganese in an ancient aquifer, kimberley formation, gale crater, mars, *Geophys. Res. Lett.* 43 (2016) 7398–7407, <https://doi.org/10.1002/2016gl069109>.
- [32] J.M. Vadillo, J.M.F. Romero, C. Rodriguez, J.J. Laserna, Effect of plasma shielding on laser ablation rate of pure metals at reduced pressure, *Surf. Interface Anal.* 27 (1999) 1009–1015, [https://doi.org/10.1002/\(sici\)1096-9918\(199911\)27:11<1009::aid-sia670>3.0.co;2-2](https://doi.org/10.1002/(sici)1096-9918(199911)27:11<1009::aid-sia670>3.0.co;2-2).
- [33] J. Diaci, J. Možina, Measurement of energy conversion efficiency during laser ablation by a multiple laser beam deflection probe, *Ultrasonics* 34 (1996) 523–525, [https://doi.org/10.1016/0041-624x\(95\)00100-h](https://doi.org/10.1016/0041-624x(95)00100-h).
- [34] P. Solana, G. Negro, A study of the effect of multiple reflections on the shape of the keyhole in the laser processing of materials, *J. Phys. D. Appl. Phys.* 30 (1997) 3216–3222, <https://doi.org/10.1088/0022-3727/30/23/006>.
- [35] W. Rapin, Hydratation de la surface de Mars partir des données du rover Curiosity, Ph.D. thesis cole doctorale Sciences de lunivers, de l'environnement et de l'espace, Toulouse, 2017.